Organic Carbon Distribution, Speciation, and Elemental Correlations within Soil Microaggregates: Applications of STXM and NEXAFS Spectroscopy

Jiamin Wan*, Tolek Tyliszczak, and Tetsu K. Tokunaga

Lawrence Berkeley National Laboratory, Berkeley, California 94720

Revised version, July 10th, 2007

ABSTRACT

Soils contain the largest inventory of organic carbon on the Earth's surface. Therefore, it is important to understand how soil organic carbon (SOC) is distributed in soils. This study directly measured SOC distributions within soil microaggregates and its associations with major soil elements from three soil groups (Phaeozem, Cambisol, and Ultisol), using scanning transmission X-ray microscopy (STXM) and near-edge X-ray absorption fine structure (NEXAFS) spectroscopy at a spatial resolution of 30 nm. Unlike previous studies, small intact soil microaggregates were examined directly in order to avoid preparatory procedures that might alter C speciation. We found that SOC exists as distinct particles (tens to hundreds of nm) and as ubiquitous thin coatings on clay minerals and iron-oxides coatings. The distinct SOC particles have higher fractions of aromatic C than the coatings. NEXAFS spectra of the C coatings within individual microaggregates were relatively similar. In the Phaeozem soil, the pervasive spectral features were those of phenolic and carboxylic C, while in the Cambisol soil the most common spectral feature was the carboxyl peak. The Ultisol soil displayed a diffuse distribution of aromatic, phenolic, and carboxylic C peaks over all surfaces. In general, a wide range of C functional groups coexist within individual microaggregates. In this work we were able to, for the first time, directly quantify the major mineral elemental (Si, Al, Ca, Fe, K, Ti) compositions simultaneously with C distribution and speciation at the nm to μm scale. These direct microscale measurements will help improve understanding on SOC-mineral associations in soil environments.

INTRODUCTION

Soil organic carbon (SOC) is the largest reservoir of organic carbon on Earth's surface. Understanding factors controlling SOC stability is critical to predicting changes in the global C balance and its broader environmental consequences (KWON and SCHNOOR, 1994; LAL, 2004; LAL et al., 2004). Humic substances and SOC have been studied extensively over the past century (HEDGES and OADES, 1997; HUANG and SCHNITZER, 1986; STEVENSON, 1994). Because humic substances contain disordered mixtures of a variety of functional groups (carboxyl, carbonyl, amino, phenol, and others) on aliphatic and aromatic linkages, they exhibit amphiphilic and amphoteric behavior. Although earlier studies led to depictions of very large (> 10 kDa) polymers, various lines of evidence now indicate that individual structures are smaller (0.1 to 1 kDa), and that they form into larger, transient micellular associations that can contain biomolecules (SUTTON and SPOSITO, 2005). The long-term persistence of the refractory fraction of SOC is puzzling in macroscopically aerobic soils in view of the thermodynamic drive to oxidize C. Several factors are believed to contribute to SOC stabilization, including physical protection, association with mineral phases, and chemical recalcitrance (BALDOCK and SKJEMSTAD, 2000; SOLLINS et al., 1996). Given the fact that SOC is oxidized within much shorter times when directly accessible to microorganisms and their extracellular enzymes, it is inferred that physical protection from these agents by restrictive micropores is important in soils (KRULL et al., 2003; ROVIRA and GREACEN, 1957; SIX et al., 2004). The recalcitrant SOC fraction has been found to be well correlated with the amorphous and poorly crystalline oxide (allophane, imogolite, ferrihydrite) fraction in soils (MIKUTTA et al., 2005; TORN et al., 1997).

Other studies show general correlations between SOC retention and the fine solids fraction (clay minerals and Fe-oxides) (EUSTERHUES et al., 2003; EUSTERHUES et al., 2005; KAISER and GUGGENBERGER, 2003). Over much longer time scales, intrinsic chemical recalcitrance appears to allow fractions of highly aromatic black carbon particles to resist oxidation for thousands of years (KRULL et al., 2003; LEHMANN et al., 2005; PESSENDRA et al., 2001).

The macroscopic scale at which most SOC measurements are made has prevented conclusive identification of dominant associations on specific minerals in natural soils. Even studies of very small quantities of soils remain effectively bulk analyses when SOC associations with diverse minerals are not determined at the scale of individual grains. Without obtaining such direct, grain-scale understanding obtained from natural samples, the mechanistic foundation for SOC-mineral stabilization will remain lacking. Recent microscopic and microspectroscopic analyses are beginning to address the issue of SOC-mineral associations (BENZERARA et al., 2005; CHENU and PLANTE, 2006; LEHMANN et al., 2005; SCHUMACHER et al., 2005), and may eventurally provide a basis for building more robust models of larger scale C cycling. Advantages of soft X-ray methods (STXM and NEXAFS) over TEM-EELS for studies of C speciation have been demonstrated (BRAUN et al., 2005). Previous applications of the STXM to SOC have yielded analyses of C functional group speciation (LEHMANN et al., 2005; SCHUMACHER et al., 2005). However, most synchrotron beamlines optimized for soft X-ray spectromicroscopy for C speciation do not have sufficient flux at higher energies to quantify Al and Si, which are by far the most abundant mineral cations in soils. Using the Beamline 11.0.2 (KILCOYNE et al., 2003) at the Advanced Light Source (ALS), Lawrence Berkeley National Laboratory, this study was able to quantify the distribution of major elements in mineral particles simultaneously with determinations of spatial distributions of SOC and SOC functional groups at

the grain surface scale (tens of nm up to 10 μm) within soil microaggregates. This scale is the natural and relevant one at which to compare SOC partitioning to fine soil aggregates of different mineralogy. Another technical difficulty encountered in studies conducted at this scale is that of making thin sections (≤100 nm) of soil microaggregates. Soil microaggregates contain both extremely soft SOC and hard minerals, such that the fixing medium must imbibe into the nanopore networks of both SOC and minerals, then harden in order to permit microtome cutting (LEHMANN et al., 2005). Possible alteration of C speciation during preparation of thin sections remains to be determined. In this study we took a different approach that circumvented the need to fix, mill, or cut microaggregates. Soil microaggregates were simply air-dried, sieved, and analyzed with the STXM to obtain maps of SOC speciation and associations with major elements within individual mineral particles at a spatial resolution of 30 nm.

EXPERIMENTAL

Soils and Sample Preparation

Samples selected for this study come from three soils, well characterized in previous investigations on SOC. Some important bulk soil properties are summarized in Table 1, and more detailed characterization of bulk properties are provided in the references associated with each soil. The Phaeozem sample used in this experiment is from a German deciduous forest soil of basalt parent rock, with a clay fraction that is primarily smectite (27% clay, 4% silt, 24% sand) (KLEBER et al., 2005; SIREGAR et al., 2005). The bulk soil cation exchange capacity is 38 $cmol_c kg^{-1}$, its specific surface area is 37 $m^2 g^{-1}$, and a pH value of 6.0 was measured from a soil water extract at a 1:1 soil to water ratio. The Cambisol sample is from a German coniferous

102 forest soil developed from gneiss (KLEBER et al., 2005), with vermiculite, kaolinite, and illite as
103 dominant clay minerals (30% clay, 30% silt, 40% sand), and is the most acidic soil (pH 4.2)
104 included in this study. The soil sample has a cation exchange capacity of 75 $cmol_c kg^{-1}$, and a
105 specific surface area of 23.0 $m^2 g^{-1}$. An Ultisol sample was obtained from a temperate forest soil
106 in Tennessee (USA) formed on shale saprolite. This soil was from the Background Site used by
107 researchers in the U.S. Department of Energy's Natural and Accelerated Bioremediation
108 Research Program (www.esd.ornl.gov/nabirfrc). After sieving (2 mm), the sample contained
109 12% clay (primarily illite), and 43% and 45% silt and sand, respectively. The bulk soil cation
110 exchange capacity is 30 $cmol_c kg^{-1}$, and the pH of its soil water extract is 6.2.
111 The < 2 mm soil particles were further sieved to remove the greater than 43 μm fraction.
112 To minimize the disturbance imposed on particle assemblages used for microspectroscopic
113 analyses, no further treatments were applied to the < 43 μm soil particles. Soil particles were
114 supported on silicon nitride (Si_3N_4) windows (1 mm^2, 200 nm thick). The air-dried and sieved
115 particles were deposited onto Si_3N_4 windows (no chemicals used), then gently shaken to remove
116 the largest particles (typically > 10 μm, based on sizes of microaggregates remaining during
117 SXTM measurements), and the Si_3N_4 window was placed on the STXM stage. Although this
118 procedure does not preserve spatial relations among large numbers of individual mineral grains
119 (original macroaggregate structure), it does retain small microaggregates that are themselves
120 stable associations of colloid-size particles including natural nanoparticles. This procedure has
121 the advantage of avoiding exposure of samples to potentially harsh physicochemical
122 disturbances. Thus, elemental associations and chemical speciation within individual particles
123 and small assemblages of particles remain practically undisturbed.
124

Scanning Transmission X-ray Microscope (STXM)

The scanning transmission X-ray microscope (STXM) is a synchrotron-based, soft X-ray microspectroscopic instrument that permits chemical mapping of thin specimens. In order to obtain maps of major mineral forming elements along with C maps, STXM measurements in this study were obtained on the Molecular Environmental Sciences Beamline 11.0.2 (KILCOYNE et al., 2003) at the Advanced Light Source (ALS), Lawrence Berkeley National Laboratory. Photons are admitted to the STXM chamber through a Si_3N_4 window and focused onto the sample by a zone plate with a working distance of 0.5 to 9 mm, depending on photon energy. The available energy range on Beamline 11.0.2 is 90-2150 eV. This unusually wide STXM energy range is essential for understanding C associations with soil particles because it allows quantification of all major mineral cations (most notably Al and Si). An order-selecting aperture is placed between the zone plate and the sample. The sample is scanned relative to the focused X-ray beam, and the transmitted intensity is recorded as a function of sample position using a scintillator with photomultiplier tube or a photodiode. The zone plate can focus the beam down to a spot size of 30 to 50 nm. The smallest resolvable features are about 25 nm. Several different zone plates are used depending on photon energy, required spatial resolution and minimum working distance. The maximum energy resolution $E/\Delta E$ is better than 7500, and a resolving power better than 3000 is achieved at a photon flux of 10^8-10^9 per second in the sub-50 nm focused beam at energies of about 200-1,600 eV. The maximum raster scan range is 20x4 mm, while the minimum step size is 2.5 nm. Images with up to 3000 x 2000 pixels can be acquired at any spatial size regime meeting these limits. The very wide dynamic range of the spatial scanning system, achieved with continuous interferometric feedback of positioning with an accuracy of 5 nm, is a very powerful aspect of this STXM.

148 Regions on the Si_3N_4 window supporting particles of suitable size were located under low
149 magnification (e.g., 50 to 500 μm field of view, 500 nm pixels, 0.5 ms dwell time) during initial
150 scanning on the STXM with the monochromatic beam set at 288 eV (just above the C K-edge
151 electron binding energy). The optical density [OD = $\log(I_o/I)$, where I_o is the background photon
152 flux transmitted through the Si_3N_4 window measured within a clean area on the same Si_3N_4
153 window, and I is the photon flux transmitted through a region within the sample] was used as an
154 initial screening criterion for selecting particles. Regions with OD > 2 were too thick to obtain C
155 maps. In general, microaggregates with lateral dimensions greater than several μm were usually
156 too thick to permit significant transmission of soft (low energy) X-rays, thus were too thick to
157 obtain quantitative elemental maps and chemical speciation. Using this constraint, small areas
158 (typically 20 to 70 μm^2) were selected on the Si_3N_4 windows containing particles having suitable
159 thickness for detailed mapping and microspectroscopic measurements. The possible scale (size)
160 dependence of SOC speciation and SOC:mineral mass ratios is beyond the scope of this study,
161 but is important in relating bulk soil properties to these measurements. Particles were then
162 scanned at higher magnification over a series of closely spaced energy steps using stack mode
163 (JACOBSEN et al., 2000) to map K edge absorption spectra for C, over the energy range of 280 to
164 300 eV. This energy range was subdivided in order to collect spectra with smaller energy steps
165 (0.10 eV) over the region associated with the main resonance peaks (284.0 to 289.0 eV), and
166 larger steps (0.25 to 0.30 eV) elsewhere. These stack measurements for C NEXAFS were
167 obtained with dwell times of 2 ms or less, and with pixel sizes from 40 to 80 nm. Maps of total
168 C distributions were then obtained using a pixel size of 25 nm, as differences of 2 absorption
169 images recorded with monochromatic X-ray energies of 280 and 288.4 eV for background and C
170 absorption, respectively. The absorption images were converted to OD images before

subtraction. After obtaining C spectra and maps, STXM maps of other elements were collected at the same pixel size. Because a main objective of this study was to identify associations of SOC with specific soil solids, K-edge OD maps of Al and Si, and L-edge OD maps of K, Ca, and Fe were obtained over the same areas that C spectra and maps were collected. In addition, L-edge maps of Ti were collected to test the hypothesis that this element would occur primarily as highly localized TiO_2 particles. These maps were obtained by subtracting below-edge OD maps for each element from its corresponding above-edge OD map. Carbon NEXAFS stack alignment and analyses, and alignment of background and edge maps of other elements were done using aXis2000 (HITCHCOCK, 2006). In addition, individual elemental maps were aligned in aXis2000 by assigning common coordinates to distinct image features. Photon energies and other parameters used for elemental mapping are listed in Table 2. For determining carbon speciation, functional groups, resonance peak energy ranges, electron transitions, and literature sources are listed in Table 4.

RESULTS AND DISCUSSION

Elemental Maps

Maps of elemental distributions within microaggregates from the Phaeozem, Cambisol, and Ultisol are shown in Figure 1. The overall morphology of each microaggregate is shown in the upper left panel for each sample. These black and white STXM images are OD maps obtained at 710 eV, just above the Fe L_{III} edge. The rainbow scale color maps represent distributions of relative elemental concentration (mass per unit area), with lowest values in dark

194 purple (black = zero), and highest values from each data set in red. The OD values from which
195 these maps were derived are presented in the following section. While the elemental maps are
196 presented in order of increasing atomic number (Z), the X-ray energies used for these maps are
197 not progressively increasing with Z because both K- and L-edges were used (Table 2). These
198 images show considerable chemical heterogeneity within small microaggregates, and individual
199 particles of different chemical compositions are often visible with characteristic sizes in the 100
200 nm to 1 μm range (30 nm resolution). Because the lowest energies used for mapping are for C,
201 and because heavier elements in minerals efficiently absorb X-rays in many regions of these
202 maps, C is not quantitatively mapped over all regions. Regions that have relatively thick mineral
203 particles will appear devoid of C simply because of insufficient X-ray transmission at the C K-
204 edge. The two Cambisol particles with greatest Al and Si thickness only show their outlines in
205 the C map; most likely because C coatings are only detectable along perimeters and not visible
206 on bulk surfaces of thick, strongly absorbing grains. Despite this limitation, the maps from these
207 samples each show broadly dispersed and locally concentrated (thick) distributions of C within
208 soil microaggregates, consistent with earlier findings (CHENU and PLANTE, 2006). One unique
209 and important advantage utilized in the present ALS 11.0.2 STXM-based study is that C
210 distributions can be mapped along with major mineral elements.
211 Maps of major mineral elements Al, Si, K, Ca, and Fe, and the minor element Ti in the
212 three samples are also shown in Figure 1. In all of these samples Ti occurs independent of other
213 metals, primarily as very sparsely distributed sub-micron particles, consistent with refractory
214 rutile or anatase (both TiO_2). The prevalence of Al, Si, and Fe, particularly Al and Si, in these
215 maps is consistent with the fact that these elements are most common in soils, especially in the

clay size fraction (< 2 μm) dominated by aluminosilicate clays and Fe-(hydr)oxides. The elemental correlations of these image maps will be discussed in the following sections.

Correlations Between Elements

The extent to which C and other elements are spatially correlated was examined by aligning each elemental OD map to common reference features using aXis2000, then comparing OD values on a pixel-by-pixel basis to determine correlation coefficients among different elements. Plots of some elemental correlations are shown in Figures 2-4, and correlation coefficients between all elemental OD pairs are provided in Tables 3a-c. It should be kept in mind that these correlations are relative to the pixel scale, which is nominally 30 nm by 30 nm along the mapping plane, and highly variable in thickness. As noted previously, thicknesses at most locations shown are less than 100 nm, and the few thicker regions are prohibitively absorbing to map elements other than Al and Si. In the elemental correlation plots for C with Al, Si, and Fe, axes for estimated thickness of SOC, Al_2O_3, SiO_2, and Fe_2O_3 have been included to indicate approximate thicknesses of individual components. These thickness estimates were obtained by dividing OD values by the product RE$\cdot\mu\cdot f\cdot\rho$ for the element of interest, where μ is the difference between the mass absorption coefficient above and below the absorption edge (g^{-1} cm^2), RE is the resonance enhancement factor (dimensionless), f is the mass fraction of the element within the solid phase, and ρ (g^{-1} cm^2) is the solid phase density (Table 2). Based on this approach, thicknesses of nearly all SOC in these maps are less than 100 nm. The regions with thicker C appear to be distinct SOC particles rather than coatings on mineral surfaces (Figure 1). Oxides of the major mineral elements Al and Si each exceeded 300 nm in thickness in the Cambisol sample, with their thicker regions interfering with mapping of C and other elements.

239 STXM maps from the Phaeozem reflect moderate correlations of C with Al, Si, and Fe
240 (Figure 2a-c). The C-Fe correlation plot (Figure 2c) may actually reflect several different C
241 associations; with Fe (hydr)oxides, with Fe-substituted aluminosilicates, and locations that have
242 both C and Fe on a common substrate (e.g., an aluminosilicate). Figure 2f shows that for this
243 sample, even Ca is better correlated to C than the aforementioned elements. Based on typical
244 values of their cation exchange capacities, Ca^{2+}-saturated humic acids and smectites both contain
245 about 2 mass% Ca. Although Ca^{2+} undoubtedly occupies a significant fraction of the cation
246 exchange sites in SOC, the Ca/C ratios are about an order of magnitude greater than that
247 attributable to cation exchange. Spectroscopic evidence ruling out $CaCO_3$ as an explanation for
248 C-Ca correlations in this sample is discussed later. In the case of the Cambisol maps, some
249 associations between C and mineral cations are obscured by the presence of very thick
250 aluminosilicate particles, such that the C correlation plots (Figure 3) and correlation coefficients
251 (Table 3b) are less informative. All areas within the Ultisol maps were thin enough to examine C
252 associations with mineral cations, and correlations with Al, Si, and Fe were nearly equally strong
253 (Figure 4a-c, and Table 3c). A number of other element-element data pairs had only very weak
254 correlations (Tables 3a-c).

255 Upon inspecting the various elemental correlations (Figures 2-4 and Tables 3a-c), it is
256 clear that those between Al and Si OD values are the strongest. This resulted from the
257 prevalence of aluminosilicates in the clay-size fractions of these soils, and because Al and Si are
258 mapped at the highest (most penetrating) X-ray energies. Molar ratios of Si:Al were calculated
259 by factoring their atomic weights into their REμ ratios, and plotted on the Si-Al correlation
260 graphs (Figures 2d, 3d, and 4d). In the Phaeozem, the STXM data are in good agreement with
261 2:1 ratios, expected based on the predominance of smectite in its clay fraction (Table 1). The

Cambisol Al and Si data correlated very well with the 1:1 line, within the range possible for kaolinite and vermiculite (DIXON and WEED, 1989), two dominant clay minerals in the bulk soil (Table 1). The Si:Al ratios obtained for the Ultisol specimen are in good agreement with 1.7:1, typical of illite (DIXON and WEED, 1989). The possibility that illite, the main mineral phase in the bulk Ultisol (Table 1), is indicated by the measured Si:Al ratios measured in this sample is further supported by the good correlations between K, Al, and Si, with ratios typical for illite. The measured K-Si ratios (Figure 4f) cluster around the range of 5.4 expected for illite (DIXON and WEED, 1989).

The OD values for Fe are well correlated to both Al and Si in the maps obtained on suitably thin samples. In the Phaeozem (Table 3a) and Ultisol (Table 3c), Fe correlation coefficients with Al and Si all exceeded 0.82. The Al:Fe ratios were approximately 2:1 in the Phaeozem (Figure 2e), and 3:1 in the Ultisol (Figure 4e). These fairly linear relations and moderately high Fe fractions may be primarily attributable to Fe substitutions for Al in gibbsite sheets within 2:1 clays. For comparison, Al:Fe ratios of about 3:1 for montmorillonite, and about 3.2 to 5.1 for illite have been reported (DIXON and WEED, 1989). Fe-(hydr)oxide coatings on aluminosilicates may also contribute to this correlation. Because of excessive thickness, Fe relations with Al and Si could not be examined for the Cambisol sample (e.g., Figure 3e).

Carbon speciation

Data presented up to this point have addressed spatial distributions of C and its pixel-scale associations with other elements, but not C speciation. Spatially resolved C speciation can reveal organic versus inorganic C, forms of SOC associated with soil minerals, and the extent of humification. Carbon NEXAFS spectra from specific locations within maps and for whole

285 specimens are presented in Figures 5-7. The dashed vertical lines within vertical shade bars in
286 the plots of spectra indicate midrange values and ranges of energies, respectively, for peaks
287 associated with specific C functional groups (Table 4). Also appearing in the higher energy
288 range of these spectra are peaks from L_{III} and L_{II} edges of potassium. Absorption intensities are
289 presented directly as OD values, but offset vertically to facilitate comparisons.

290 The distribution of SOC in the Phaeozem is both diffuse and locally concentrated in
291 chemically distinct particulate forms (Figure 5). Although the two most concentrated C regions
292 are attached to the mineral particles forming the microaggregate framework, they do not appear
293 to coat Al-, Si-, or Fe-containing grains (Figure 1). Both of the C-rich regions are 400 to 600 nm
294 in lateral extent (Figure 1), and about 100 nm thick (Figure 2). Region 1 has distinct peaks at
295 285.1 eV (aromatic C) and 288.0 eV (0.2 eV below the peptide peak energy), and a shoulder at
296 286.7 (phenolic, ketonic C). In contrast, the absorption edge for region 2 begins to rise about 1
297 eV below the aromatic C energy in the vicinity of a peak reported for quinonic C, exhibits a
298 broad peak at 285.8 eV, and has additional peaks at 288.5 (carboxylic C) and 290.3 eV
299 (carbonate/carbonyl C). Quinonic C occurs during decomposition of lignin (STEVENSON, 1994),
300 and thus may be more prevalent in larger SOC particles undergoing humification. The nature of
301 the broad peak at 285.8 eV and the high Ca concentration within region 2 are unknown. $CaCO_3$
302 is unlikely to be present because of the slightly acidic soil pH, and because of the weakness of
303 the resonance at 290.3 eV relative to that of calcite (BENZERARA et al., 2005). The ubiquitous
304 occurrence of this resonance at 290.3 eV and lack of C-Ca correlation suggest that this weak
305 peak is indicative of some other carbonate or carbonyl groups in SOC. Other regions on this
306 Phaeozem sample exhibited spectra that were similar to that of the whole specimen, with weak to
307 moderate peaks at 285.1, 286.7, 288.5, and 290.3 eV.

Carbon NEXAFS were obtained over most of the Cambisol sample, excluding the regions with thickest Al and Si (particles "A" and "B" in the Figure 6 images). Like the Phaeozem sample, C is distributed very heterogeneously, with locally concentrated regions each having different NEXAFS spectra. Region 1 is the only location on this sample having a peak at 285.1 eV (aromatic C), followed by a gradual rise in the absorption edge, and appears to be a distinct attached particle (≈ 200 to 500 nm) rather than a coating on a mineral grain (Figure 1). Both regions 2 and 3 occur as SOC coatings on a mineral grain, and have C NEXAFS with peaks at 286.7 eV (phenolic C) and at 288.2-288.5 eV (peptidic, carboxylic C). All other regions (regions 4 and 5 are shown in Figure 6, but 3 other coating regions were also checked) of this sample only had peaks in the 288.2-288.5 eV range, and were similar to the spectrum of the whole sample.

Carbon NEXAFS spectra from the Ultisol sample were generally weaker in intensity because of lower C concentrations. In this sample, C was relatively uniformly distributed, with no large (>100 nm) particles detected (Figure 1). The C NEXAFS spectra were similar throughout the sample, containing peaks at 285.1, 286.7, and 288.5 eV (Figure 7). Although total C concentrations are low in this sample, the resonance from aromatic C (285.1 eV) was strong. More intense peaks at 297 and 300 eV were obtained because of the higher K contents in this illitic soil.

Collectively, the C NEXAFS maps display both variability and homogeneity within individual microaggregates. The variability was largely associated with localized SOC-rich regions within microaggregates. These SOC-rich regions appear to be distinct particles several hundred nm in size, that have higher fractions of aromatic C than their surroundings. Outside of these locally C-rich locations, C NEXAFS spectra within individual microaggregates were

relatively similar. In the Phaeozem, the pervasive NEXAFS features were those of phenolic and carboxylic C, while in the carboxylic peak was most common within the Cambisol sample. As previously noted, the Ultisol sample displayed a diffuse distribution of aromatic, phenolic, and carboxylic C peaks over all surfaces.

Implications

The scientific basis for predicting changes in soil OC storage is under active development, and is a critical component for carbon management and for predicting climate change. Quantifying grain-scale SOC distribution may help test mechanistic models for predicting larger scale SOC retention in soils. Using the wide energy range accessible by the ALS beamline 11.0.2 STXM, this study provided direct determinations of SOC microscale distribution, speciation and spatial associations with major soil mineral elements Si, Al, Ca, K, Ti, and Fe. Diverse C functional groups occurred together, and SOC was distributed as discrete particles and coatings on soil minerals. This study also demonstrated the viability of the approach of sample preparation through selecting particles with suitable thicknesses, instead of making thin sections from soil microaggregates. The selectivity for particle thicknesses ≤ 100 nm is not expected to affect conclusions concerning SOC associations with mineral surfaces because soil surface area is largely associated with finer colloidal particles. This method is especially attractive because of its simplicity and because it minimizes possible changes introduced with physical-chemical processing. Like many other microscale analyses in soils and heterogeneous media in general, large numbers of local measurements are required in order to quantify microscopic distributions underlying macroscopic properties. Studies of more soil types, with multiple samples analyzed using different approaches will help develop a clearer

354 understanding of specific SOC-mineral associations. Thus, the simplicity of approach presented
355 here makes it conducive to obtaining large numbers of measurements, and is complementary to
356 other more laborious preparation methods.
357
358 **ACKNOWLEDGMENTS**
359
360 We thank Markus Kleber, Margaret Torn, and Asmeret Berhe of LBNL for helpful discussions
361 and for providing soil samples. We appreciate Yongman Kim's help for soil total organic carbon
362 analyses. We appreciate Glenn Waychunas for internal review of the manuscript. We thank the
363 three anonymous reviewers and the Associate Editor Donald Sparks for their constructive review
364 comments. Funding of this work was provided by the Geosciences Division of the Basic Energy
365 Science (BES) program, under the Office of Science, U.S. Department of Energy. This work
366 was conducted at beamlines 11.0.2 and 5.3.2 at the Advanced Light Source, Lawrence Berkeley
367 National Laboratory, which is supported by the Office of Science, Office of Basic Energy
368 Sciences, Division of Materials Sciences, and Division of Chemical Sciences, Geosciences, and
369 Biosciences of the U. S. Department of Energy under contract DE-AC03-76SF00098.
370

370 **LITERATURE CITED**

371

372 Baldock J. A. and Skjemstad J. O. (2000) Role of the soil matrix and minerals in protecting
373 natural organic materials against biological attack. *Organic Geochemistry* **31**, 697-710.

374 Benzerara K., Yoon T. H., Menguy N., Tyliszczak T., and Brown G. E., Jr. (2005) Nanoscale
375 environments associated with bioweathering of a Mg-Fe-pyroxene. *Proceedings of the*
376 *National Academy of Sciences* **102**(4), 979-982.

377 Benzerara K., Yoon T. H., Tyliszczak T., Constantz B., Spormann A. M., and Brown G. E., Jr.
378 (2004) Scanning transmission X-ray microscopy study of microbial calcification.
379 *Geobiology* **2**, 249-259.

380 Boyce C. K., Cody G. D., Feser M., Jacobsen C., Knoll A. H., and Wirick S. (2002) Organic
381 chemical differentiation within fossil plant cell wals detected with X-ray
382 spectromicroscopy. *Geology* **30**, 1039-1042.

383 Braun A., Huggins F. E., Shah N., Chen Y., Wirick S., Mun S. B., Jacobsen C., and Huffiman G.
384 P. (2005) Advantages of soft X-ray absorption over TEM-EELS for solid carbon studies:
385 a comparative study on diesel soot with EELS and NEXAFS. *Carbon* **43**, 117-124.

386 Chenu C. and Plante A. F. (2006) Clay-sized organo-mineral complexes in a cultivation
387 chronosequence: revisiting the concept of the 'primary organo-mineral complex'.
388 *European Journal of Soil Science* **57**, 596-607.

389 Cody G. D., Ade H., Wirick S., Mitchell G. D., and Davis A. (1998) Determination of chemical-
390 structural changes in vitrinite accompanying luminescence alteration using C-NEXAFS
391 analysis. *Organic Geochemistry* **28**(7-8), 441-455.

392 Dixon J., B. and Weed S. B. (1989) *Mineral in Soil Environments.* Soil Science Society of
393 America.

394 Eusterhues K., Rumpel C., Kleber M., and Kogel-Knabner I. (2003) Stabilisation of soil organic
395 matter by interactions with minerals as revealed by mineral dissolution and oxidative
396 degradation. *Organic Geochemistry* **34**, 1591-1600.

397 Eusterhues K., Rumpel C., and Kogel-Knabner I. (2005) Stabilization of soil organic matter
398 isolated via oxidative degradation. *Organic Geochemistry* **36**, 567-575.

399 Francis J. T. and Hitchcock A. P. (1992) Inner-shell spectroscopy of p-benzoquinone,
400 hydroquinone, and phenol: Distinguishing quinoid and benzenoid structures. *Journal of*
401 *Physical Chemistry* **96**, 6598-6610.

402 Hedges J. I. and Oades J. M. (1997) Comparative organic geochemistries of soils and marine
403 sediments. *Organic Geochemistry* **27**, 319-361.

Hitchcock A. P. (2006) aXis2000. Analysis of X-ray images and spectra. *McMaster University, Hamilton, Ontario, Canada* **http://unicorn.mcmaster.ca/aXis2000.html**.

Huang P. M. and Schnitzer M. (1986) *Interactions of Soil Minerals with Natural Organics and Microbes.* Soil Science Society of America.

Jacobsen C., Flynn G., Wirick S., and Zimba C. (2000) Soft x-ray spectroscopy from image sequences with sub-100 nm spatial resolution. *Journal of Microscopy* **197**(2), 173-184.

Kaiser K. and Guggenberger G. (2003) Mineral surfaces and soil organic matter. *European Journal of Soil Science* **54**, 219-236.

Kilcoyne A. L. D., Tyliszczak T., Steele W. F., Fakra S., Hitchcock P., Frank K., Anderson E., Harteneck B., Rightor E. G., Mitchell G. E., Hitchcock A. P., Yang L., Warwick T., and Ade H. (2003) Interferometer-controlled scanning transmission X-ray microscopes at the Advanced Light Source. *Journal of Synchrotron Radiation* **10**, 125-136.

Kleber M., Mikutta R., Torn M. S., and Jahn R. (2005) Poorly crystalline mineral phases protect organic matter in acid subsoil horizons. *European Journal of Soil Science* **doi: 10.1111/j.1365-2389.2005.00706.x**, 717-725.

Krull E. S., Baldock J. A., and Skjemstad J. O. (2003) Importance of mechanisms and processes of the stabilisation of soil organic matter for modelling carbon turnover. *Functional Plant Biology* **30**, 207-222.

Kwon O.-Y. and Schnoor J. L. (1994) Simple global carbon model: The atmosphere-terrestrial biosphere-ocean interaction. *Global Biogeochemical Cycles* **8**, 295-305.

Lal R. (2004) Soil carbon sequestration impacts on global climate change and food security. *Science* **304**, 1623-1626.

Lal R., Griffin M., Apt J., Lave L., and Morgan M. G. (2004) Managing soil carbon. *Science* **304**, 393.

Lehmann J., Liang B., Solomon D., Lerotic M., Luizao F., J. K., Schafer T., and Wirick S. (2005) Near-edge x-ray absorption fine structure (NEXAFS) spectroscopy for mapping nano-scale distribution of organic carbon forms in soils: Application to black carbon particles. *Global Biogeochemical Cycles* **19**, 10.1029/2004GB002435, 2005.

Mikutta R., Kleber M., and Jahn R. (2005) Poorly crystalline minerals protect organic carbon in clay subfractions from acid subsoil horizons. *Geoderma* **128**, 106-115.

Pessendra L. C. R., Gouveia S. E. M., and Aravena R. (2001) Radiocarbon dating of total soil organic matter and humin fraction and its comparison with 14C ages of fossil charcoal. *Radiocarbon* **43**(2B), 595-601.

Rovira A. D. and Greacen E. L. (1957) The effect of aggregate disruption on the activity of microorganisms in the soil. *Australian Journal of Soil Research* **8**, 659-673.

Schumacher M., Christl I., Scheinost A. C., Jacobsen C., and Kretzschmar R. (2005) Chemical heterogeneity of organic soil colloids investigated by scanning transmission X-ray microscopy and C-1s NEXAFS microspectroscopy. *Environmental Science and Technology* **39**(23), 9094-9100.

Siregar A., Kleber M., Mikutta R., and Jahn R. (2005) Sodium hypochlorite oxidation reduces soil organic matter concentrations without affecting inorganic soil constituents. *European Journal of Soil Science* **56**, 481-490.

Six J., Bossuyt H., Degryze S., and Denef K. (2004) A history of research on the link between (micro)aggregates, soil biota, and soil organic matter dynamics. *Soil and Tillage Research* **79**, 7-31.

Sollins P., Homann P., and Caldwell B. A. (1996) Stabilization and destabilization of soil organic mateer: mechansms and controls. *Geoderma* **74**, 65-105.

Stevenson F. J. (1994) *Humus Chemistry, 2nd Edition*. Wiley.

Sutton R. and Sposito G. (2005) Molecular structure in soil humic substances: The new view. *Environmental Science and Technology* **39**, 9009-9015.

Torn M. S., Trumbore S. E., Chadwick O. A., Vitousek P. M., and Hendrick D. M. (1997) Mineral control of soil organic carbon storage and turnover. *Nature* **389**, 170-173.

459 **TABLES**

460

461 **Table 1.** Soil samples and characteristics. Depths are relative to the mineral soil surface. Clay
462 mineralogy: cl chlorite, gt goethite, il illite, ka kaolinite, pl plagioclase, sm smectite, ve
463 vermiculite. The pH values are from 1:1 soil:water extracts. Fe-dith. and Fe-ox. Refer to
464 dithionite and oxalate extractable Fe (SIREGAR et al., 2005).

soil	depth	C	clay mineralogy	clay	Fe-dith.	Fe-ox.	pH
	m	%		%	%	%	
Phaeozem	0.05-0.35	3.2	sm	27	2.5	0.9	6.0
Cambisol	0.10-0.30	3.8	ve, il, ka	30	3.6	1.9	4.2
Ultisol	0.05-0.15	2.5	il > (qz,ka,cl,gt,pl)	12	4.6	0.4	6.2

465

466

466 **Table 2.** X-ray energies, differences between mass attenuation coefficients above and below the
467 absorption edge (μ), and approximate resonance enhancements (RE) used for elemental
468 mapping. *Values of μ, RE, and density □ for Al, Si, and Fe are for generic oxides $Al(OH)_3$,
469 SiO_2, and Fe_2O_3, respectively, and therefore used in this study only to estimate thicknesses. **In
470 order to estimate SOC thickness, $\rho = 1.4$ g cm^{-3} and $f = 0.58$ were used (STEVENSON, 1994). f is
471 the mass fraction of the element of interest within its solid phase.

element	edge	below-edge energy, eV	above-edge energy, eV	μ, g^{-1} cm^2	RE	ρ, g cm^{-3}	f, g g^{-1}
C	K	280.0	289.0	51,400	1	1.4**	0.58
Al	K	1,560.0	1,571.5	3,800*	2.5*	2.35*	0.35
Si	K	1,836.0	1,845.0	3,075*	5*	2.65*	0.47
K	L_2	294.0	300.0	50,000	3		
Ca	L_2	345.0	352.4	40,000	3 to 5		
Ti	L_3	456.0	458.0	27,000	3 to 6		
Fe	L_3	703.0	710.0	15,800*	5*	4.3*	0.63

472

Table 3. Correlation coefficients from pairs of OD values from different elements within maps of (**a.**) Phaeozem, (**b.**) Cambisol, and (**c.**) Ultisol.

a. Phaeozem						
	Al	**Si**	**K**	**Ca**	**Ti**	**Fe**
C	0.547	0.445	0.442	0.767	0.450	0.505
Al		0.876	0.344	0.740	0.319	0.824
Si			0.319	0.686	0.241	0.887
K				0.412	0.281	0.350
Ca					0.275	0.768
Ti						0.292

b. Cambisol						
	Al	**Si**	**K**	**Ca**	**Ti**	**Fe**
C	0.049	0.039	0.464	0.339	0.193	0.720
Al		0.987	0.258	0.198	0.094	0.365
Si			0.244	0.160	0.086	0.349
K				0.669	0.091	0.457
Ca					0.009	0.306
Ti						0.333

c. Ultisol						
	Al	**Si**	**K**	**Ca**	**Ti**	**Fe**
C	0.813	0.816	0.706	0.393	0.271	0.783
Al		0.952	0.785	0.272	0.199	0.893
Si			0.882	0.286	0.169	0.921
K				0.326	0.120	0.748
Ca					0.431	0.247
Ti						0.137

477 **Table 4.** Carbon functional groups, peak energy ranges, transitions, and literature sources.

C functional groups	Energy, eV	transition	sources
Quinonic C=O, protonated aromatic	283.7 – 284.3	1s-π*	(CODY et al., 1998; FRANCIS and HITCHCOCK, 1992; LEHMANN et al., 2005)
Aromatic C_{arom}=C_{arom} , C_{arom}=H	284.9 – 285.5	1s-π*	(BENZERARA et al., 2004; CODY et al., 1998; LEHMANN et al., 2005; SCHUMACHER et al., 2005)
Phenolic C_{arom}-OH, ketonic C=O	286.5 – 287.2	1s-π*	(BENZERARA et al., 2004; BOYCE et al., 2002; LEHMANN et al., 2005; SCHUMACHER et al., 2005)
Aliphatic C-H	287.1 – 287.8	1s-3p/σ*	(BOYCE et al., 2002; LEHMANN et al., 2005)
Amide-carbonyl (peptidic) C=O	288.2	1s-π*	(BENZERARA et al., 2004)
Carboxylic C=O, C-OH	287.7 – 288.6	1s-π*	(BENZERARA et al., 2004; BOYCE et al., 2002; LEHMANN et al., 2005; SCHUMACHER et al., 2005)
Carbonate, carbonyl C=O	290.2 – 290.5	1s-π*	(BENZERARA et al., 2005; BENZERARA et al., 2004; SCHUMACHER et al., 2005)

478

479

480

481

481 FIGURE CAPTIONS

482

483 **Figure 1.** Elemental relative distribution maps within microaggregates from the Phaeozem,
484 Cambisol, and Ultisol (rainbow color scale, with red = highest concentration). The overall
485 microaggregate outline for each sample is shown in the optical density map collected at 710 eV.

486

487 **Figure 2.** Phaeozem sample correlation plots of OD obtained from STXM maps shown in
488 Figure 1. Linear correlation coefficients for these plots and other elemental relations are
489 provided in Table 3a.

490

491 **Figure 3.** Cambisol sample correlation plots of OD obtained from STXM maps shown in Figure
492 1. Linear correlation coefficients for these plots and other elemental relations are provided in
493 Table 3b.

494

495 **Figure 4.** Ultisol sample correlation plots of OD obtained from STXM maps shown in Figure 1.
496 Linear correlation coefficients for these plots and other elemental relations are provided in Table
497 3c.

498

499 **Figure 5.** Carbon NEXAFS spectra obtained within selected areas of the Phaeozem
500 microaggregate (regions numbered 1 through 6), and for the whole sample. Spectral features
501 identified by the vertical dashed lines correspond to C in (a) quinonic, (b) aromatic, (c) phenolic,
502 (d) aliphatic, (e) peptidic, (f) carboxylic, and (g) carbonate/carbonyl functional groups. The
503 shaded gray bands indicate energy ranges attributed to each functional group (Table 4). The

peaks at the higher energies result from small amounts of K^+, and correspond to its L_3 and L_2 edges.

Figure 6. Carbon NEXAFS spectra obtained within selected areas of the Cambisol microaggregate (1 through 5), and for the whole sample. The aluminosilicate particles that are too thick for C NEXAFS measurements are labeled A and B in the maps. Spectral features identified by the vertical dashed lines correspond to C in (a) quinonic, (b) aromatic, (c) phenolic, (d) aliphatic, (e) peptidic, (f) carboxylic, and (g) carbonate/carbonyl functional groups. The peaks at the higher energies are from K^+, and correspond to its L_3 and L_2 edges.

Figure 7. Carbon NEXAFS spectra obtained within a selected area of the Ultisol microaggregate (region 1), and for the whole sample. Spectral features identified by the vertical dashed lines correspond to C in (a) quinonic, (b) aromatic, (c) phenolic, (d) aliphatic, (e) peptidic, (f) carboxylic, and (g) carbonate/carbonyl functional groups. Peaks from K^+ L_3 and L_2 edges are more intense in this sample because of the K-rich illite matrix.

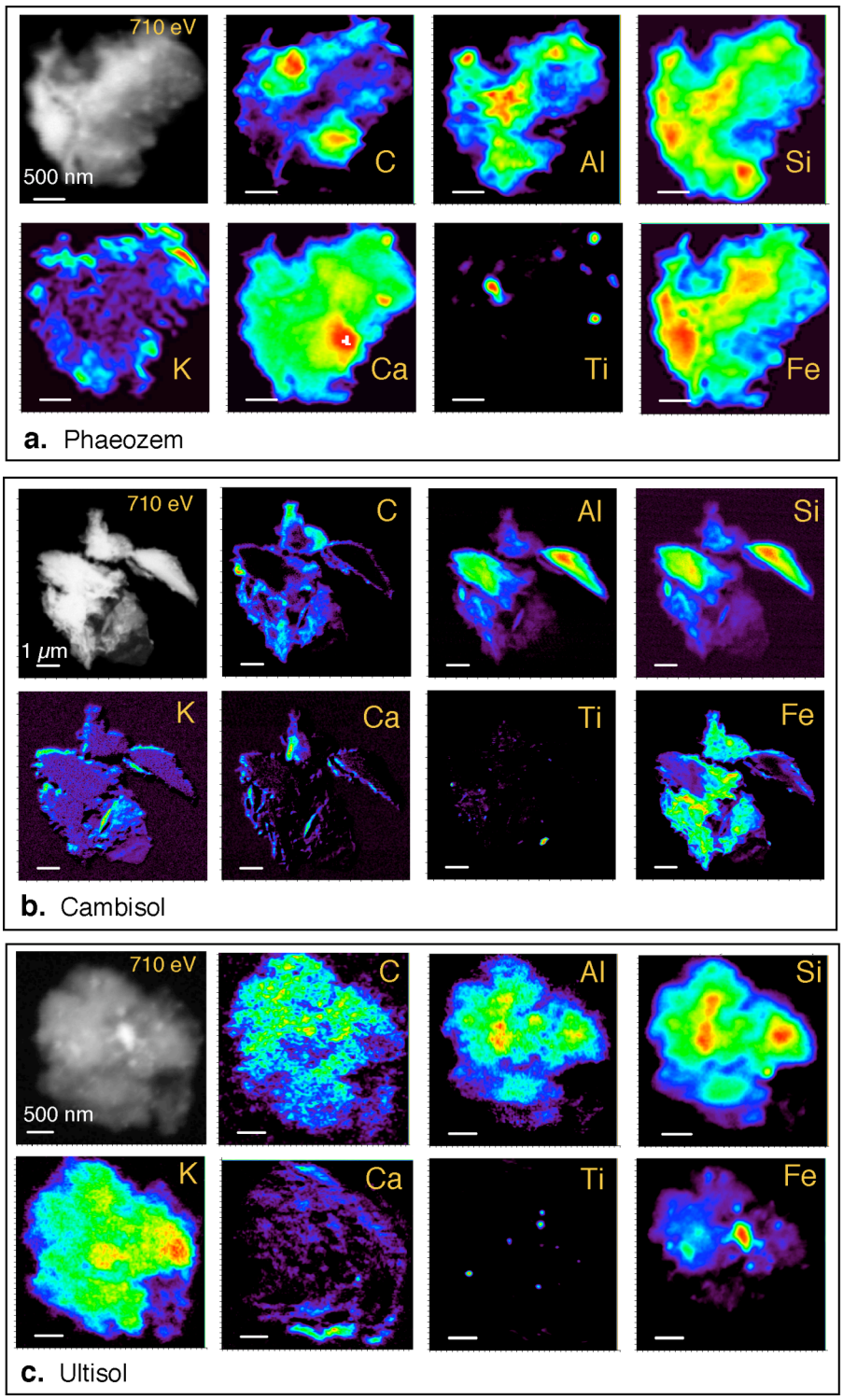

520

521

522 **Figure 1.** Elemental relative distribution maps within microaggregates from the Phaeozem,
523 Cambisol, and Ultisol (rainbow color scale, with red = highest concentration). The overall
524 microaggregate outline for each sample is shown in the optical density map collected at 710 eV.

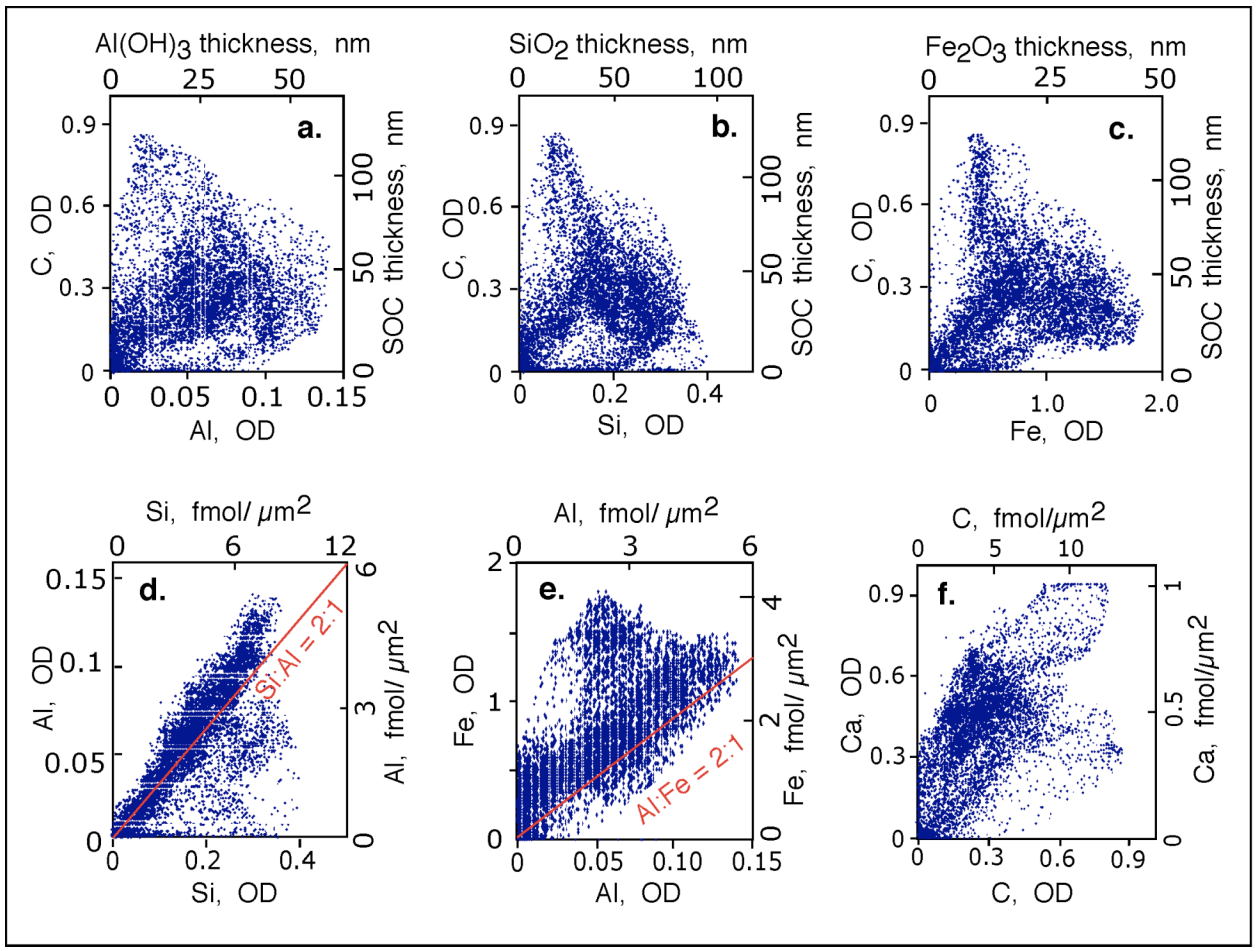

525

526

527 **Figure 2.** Phaeozem sample correlation plots of OD obtained from STXM maps shown in

528 Figure 1. Linear correlation coefficients for these plots and other elemental relations are

529 provided in Table 3a.

530

531

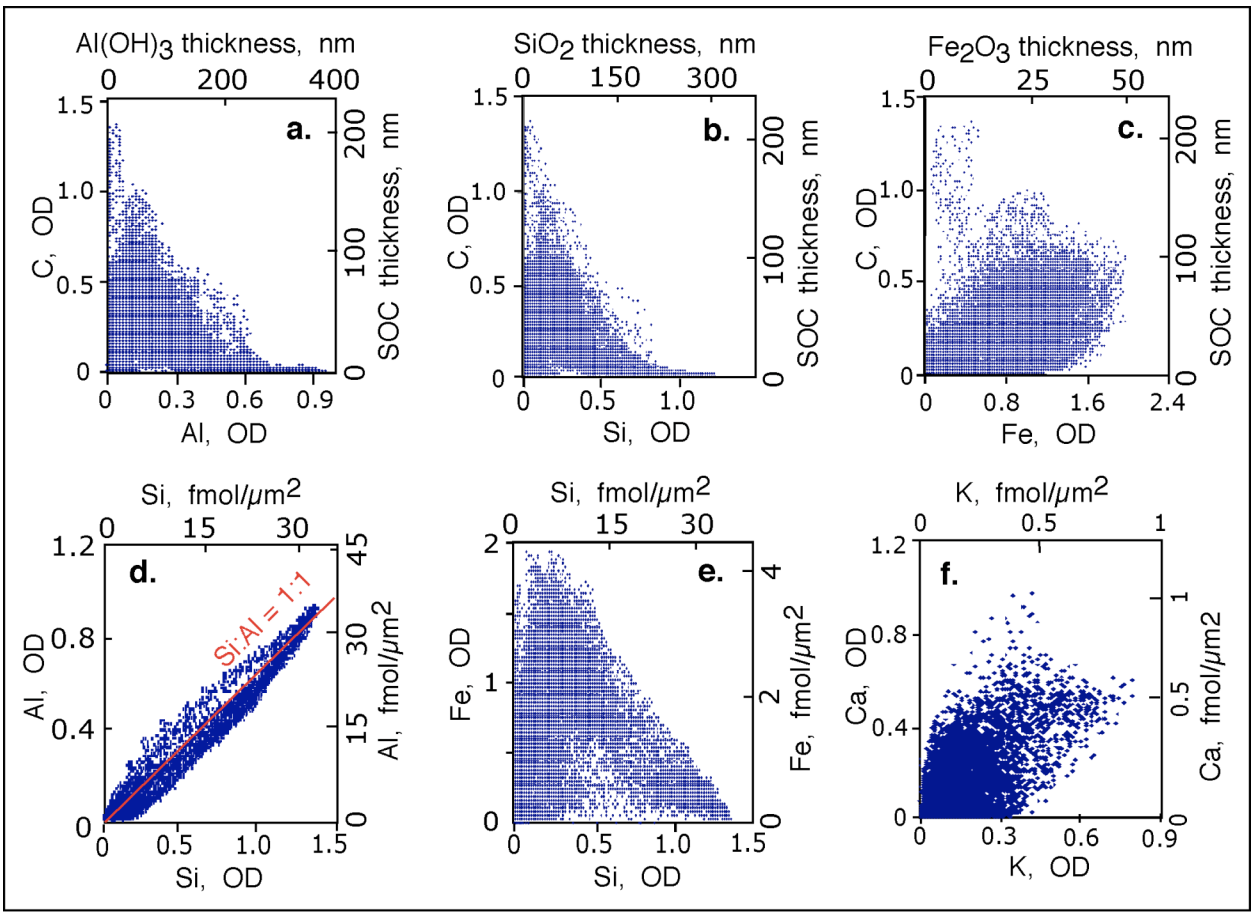

532

533

534 **Figure 3.** Cambisol sample correlation plots of OD obtained from STXM maps shown in Figure

535 1. Linear correlation coefficients for these plots and other elemental relations are provided in

536 Table 3b.

537

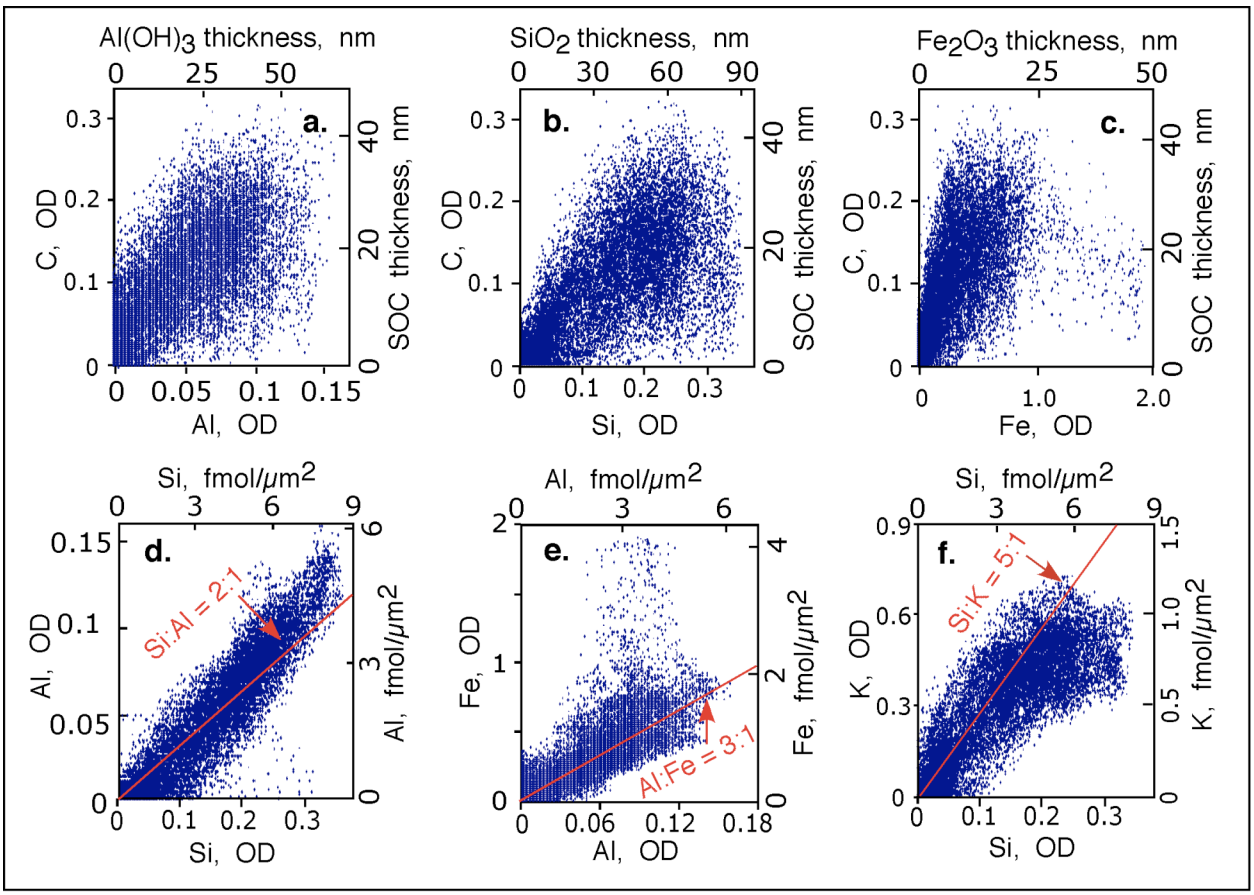

538

539

540 **Figure 4.** Ultisol sample correlation plots of OD obtained from STXM maps shown in Figure 1.

541 Linear correlation coefficients for these plots and other elemental relations are provided in Table

542 3c.

543

544

545

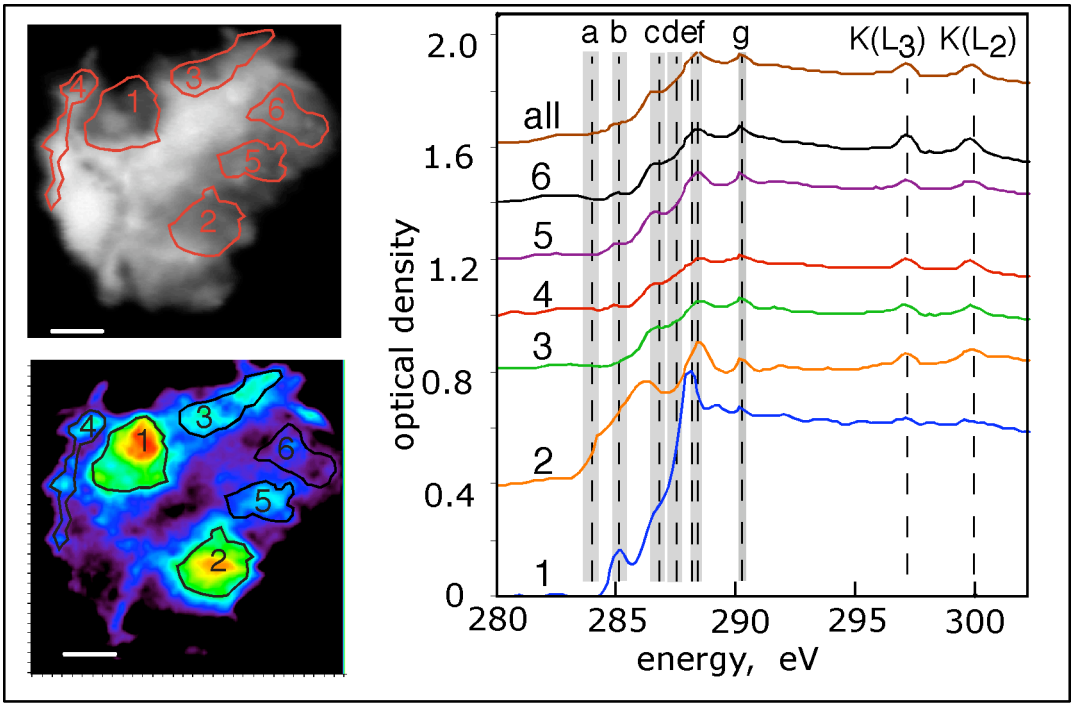

546

547

548 **Figure 5.** Carbon NEXAFS spectra obtained within selected areas of the Phaeozem
549 microaggregate (regions numbered 1 through 6), and for the whole sample. Spectral features
550 identified by the vertical dashed lines correspond to C in (a) quinonic, (b) aromatic, (c) phenolic,
551 (d) aliphatic, (e) peptidic, (f) carboxylic, and (g) carbonate/carbonyl functional groups. The
552 shaded gray bands indicate energy ranges attributed to each functional group (Table 4). The
553 peaks at the higher energies result from small amounts of K^+, and correspond to its L_3 and L_2
554 edges.

555

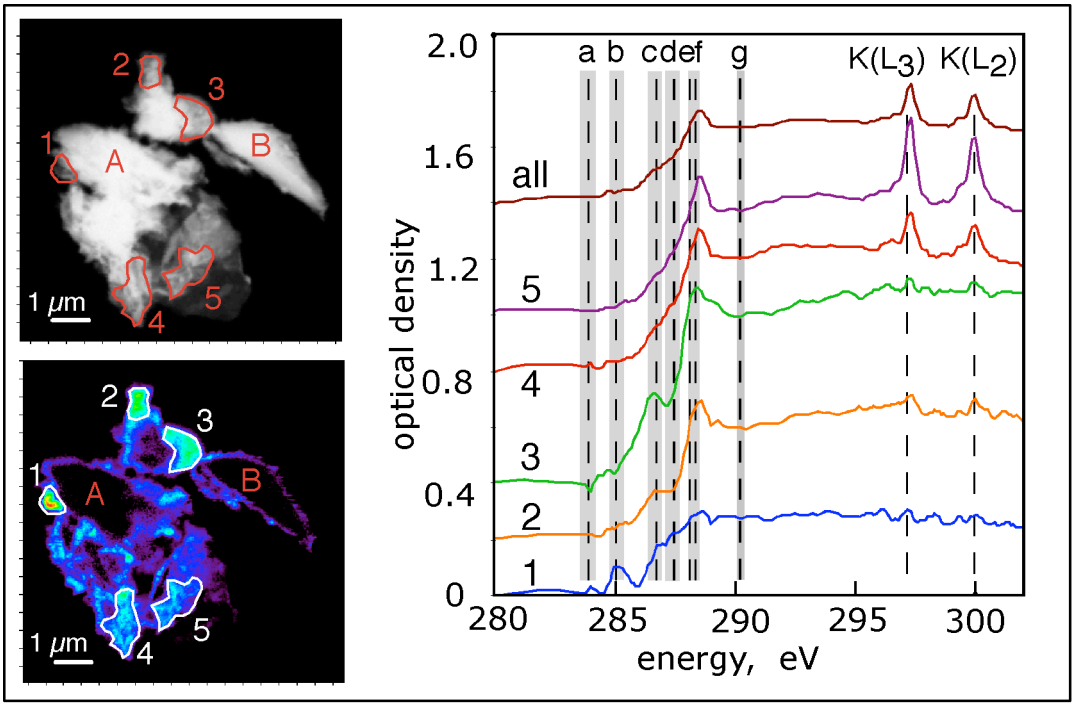

556

557

558 **Figure 6.** Carbon NEXAFS spectra obtained within selected areas of the Cambisol

559 microaggregate (1 through 5), and for the whole sample. The aluminosilicate particles that are

560 too thick for C NEXAFS measurements are labeled A and B in the maps. Spectral features

561 identified by the vertical dashed lines correspond to C in (a) quinonic, (b) aromatic, (c) phenolic,

562 (d) aliphatic, (e) peptidic, (f) carboxylic, and (g) carbonate/carbonyl functional groups. The

563 peaks at the higher energies are from K^+, and correspond to its L_3 and L_2 edges.

564

565

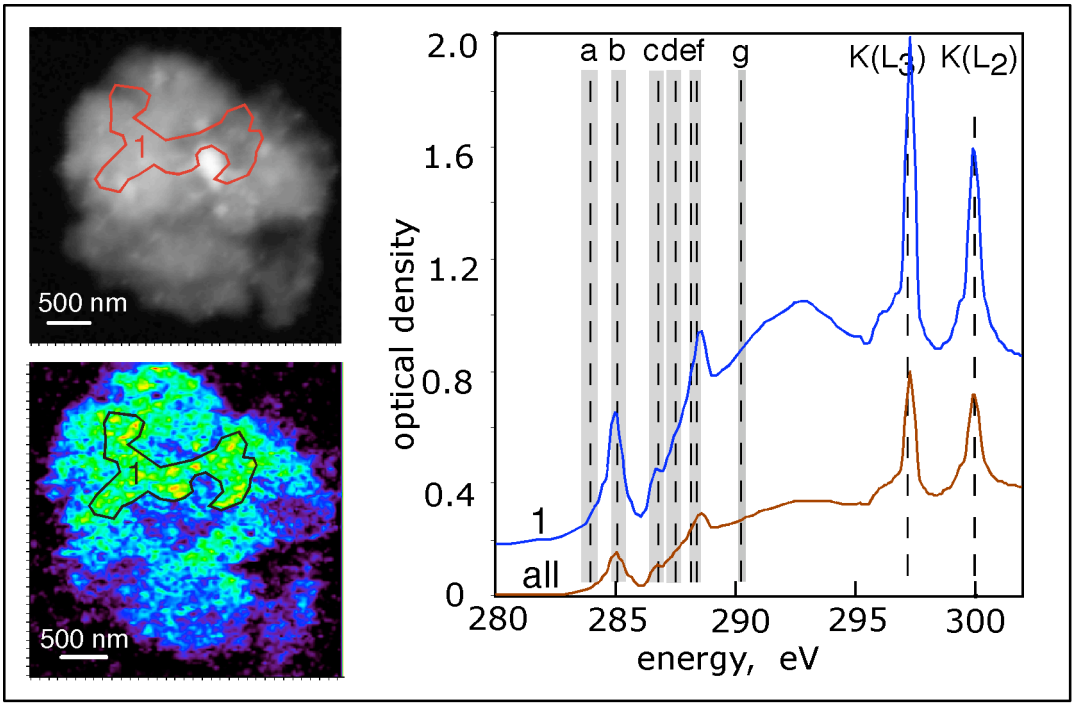

566

567

568 **Figure 7.** Carbon NEXAFS spectra obtained within a selected area of the Ultisol

569 microaggregate (region 1), and for the whole sample. Spectral features identified by the vertical

570 dashed lines correspond to C in (a) quinonic, (b) aromatic, (c) phenolic, (d) aliphatic, (e)

571 peptidic, (f) carboxylic, and (g) carbonate/carbonyl functional groups. Peaks from K^+ L_3 and L_2

572 edges are more intense in this sample because of the K-rich illite matrix.

573